3-2016

Development of High-Order P_N Models for Radiative Heat Transfer in Special Geometries and Boundary Conditions

Wenjun Ge
University of California - Merced

Michael F. Modest
University of California - Merced

Somesh Roy
Marquette University, somesh.roy@marquette.edu

Journal of Quantitative Spectroscopy and Radiative Transfer, Vol. 172 (March 2016): 98-109. DOI.

Development of High-Order P_N Models for Radiative Heat Transfer in Special Geometries and Boundary Conditions

Wenjun Ge
University of California, Merced, CA
Michael F. Modest
University of California, Merced, CA
Somesh P. Roy
University of California, Merced, CA

Highlights

- •Derivation of the 2-D Cartesian formulation for the high order spherical harmonics (PN) methods.
- •Derivation of the boundary condition of PN for the mixed diffuse-specular surfaces.
- •Derivation of the boundary condition of PN for specified radiative heat flux at the wall.
- •Derivation of the boundary condition of PN for symmetry/specular boundaries.

Abstract

The high-order spherical harmonics (P_N) method for 2-D Cartesian domains is extracted from the 3-D formulation. The number of equations and intensity coefficients reduces to (N+1)2/4 in the 2-D Cartesian formulation compared with N(N+1)/2 for the general 3-D P_N formulation. The Marshak boundary conditions are extended to solve problems with nonblack and mixed diffuse-specular surfaces. Additional boundary conditions for specified radiative wall flux, for symmetry/specular reflection boundaries have also been developed. The mathematical details of the formulations and their implementation in the *OpenFOAM* finite volume based CFD software platform are presented. The accuracy and computational cost of the 2-D Cartesian P_N are compared with that of the 3-D P_N solver and a Photon Monte Carlo solver for a square enclosure, as well as a 45° wedge geometry with variable radiative properties. The new boundary conditions have been applied for both test cases, and the boundary condition for mixed diffuse-specular surfaces is further illustrated by numerical examples of a rectangular geometry enclosed by walls with different surface characteristics.

Keywords

Radiative transfer, RTE solver, High-order spherical harmonics, Specified heat flux at the wall, Specular reflection, Partially diffuse and partially specular

1. Introduction

This note is a supplement to the research papers [1], [2], [3], [4], [5] on the development of higher-order spherical harmonics (P_N) methods for radiative heat transfer and their implementation into *OpenFOAM* [6]. A 2-D Cartesian version of the higher-order P_N methods and their Marshak boundary conditions are extracted from the 3-D P_N formulation. The Marshak boundary conditions are extended to solve problems with nonblack and mixed diffuse-specular surfaces. In addition, two special boundary conditions, i.e., specified radiative flux at the wall and interfaces of symmetry/specular reflection boundaries, for both 3-D and 2-D P_N formulations, are developed.

2. Formulation of the two-dimensional Cartesian P_N

2.1. Governing equations and boundary conditions

The formulation of the 2-D Cartesian P_N is derived from the 3-D formulation by observing the characteristics of spherical harmonics Y_n^m. As shown in [2] for general three-dimensional geometries, the radiative intensity is expanded into a sum of spherical harmonics:

$$(1)\ I(\boldsymbol{\tau},\hat{\mathbf{s}}) = \sum_{n=0}^{N}\sum_{m=-n}^{n} I_n^m(\boldsymbol{\tau})Y_n^m(\hat{\mathbf{s}})$$

where $\boldsymbol{\tau} = \int \beta_r \mathrm{d}\mathbf{r}$ is an optical coordinate, and β_r is the extinction coefficient. The upper limit N is the order of the approximation, and the spherical harmonics Y_n^m are functions of polar angle θ and azimuthal angle ψ,

$$(2)\ Y_n^m = \begin{cases} \cos(m\psi)P_n^m(\cos\theta) & \text{for} m \geq 0 \\ \sin(|m|\psi)P_n^m(\cos\theta) & \text{for} m < 0 \end{cases}$$

where P_n^m are associated Legendre polynomials [3], given by

$$(3)\ P_n^m(\mu) = (-1)^m \frac{(1-\mu^2)^{|m|/2}}{2^n n!}\frac{d^{n+|m|}}{d\mu^{n+|m|}}(\mu^2-1)^n$$

By eliminating spherical harmonics with odd n, a general three-dimensional formulation in $N(N+1)/2$ elliptical PDEs can be derived [2].

$N(N+1)/2$ boundary conditions are required and determined from the general Marshak boundary condition [7]:

(4) $$\int_{\hat{\mathbf{n}}\cdot\hat{\mathbf{s}}>0} I\bar{Y}_{2i-1}^{m} d\Omega = \int_{\hat{\mathbf{n}}\cdot\hat{\mathbf{s}}>0} I_w \bar{Y}_{2i-1}^{m} d\Omega, i = 1,2,\ldots,\frac{1}{2}(N+1), \mathrm{all relevant} m$$

Substitution of Eq. (1) in terms of local coordinates into Eq. (4) leads to

(5) $$(1+\delta_{m,0})\pi \sum_{n=0}^{N} p_{n,2i-1}^{m} \bar{I}_n^m = \int_0^{2\pi}\int_0^1 I_w \bar{Y}_{2i-1}^{m} d\bar{\mu} d\bar{\psi}$$

if I_w is diffuse, this simplifies to

(6) $$\sum_{n=0}^{N} p_{n,2i-1}^{m} \bar{I}_n^m = \delta_{m,0} p_{0,2i-1}^{0} I_w$$

The detailed derivation of the $N(N+1)/2$ boundary conditions for the 3-D P_N formulation can be found in [2], [3]. For two-dimensional Cartesian geometry in the $x-y$ plane with polar angle θ measured from the z-axis, one obtains $I(\theta,\psi) = I(\pi-\theta,\psi)$ or $I(\mu,\psi) = I(-\mu,\psi)$ for $\mu = \cos\theta$, as seen from Eqs. (2), (3), the associated Legendre polynomials $P_n^m(\mu)$ are odd functions when $(m+n)$ are odd, thus I_n^m with $(m+n)$ being odd must vanish. Since the governing equations are formulated with even n only, all terms in the governing equation with odd m vanish. Based on this, and eliminating all derivatives into the z-direction, the remaining $(N+1)^2/4$ governing equations for order N are

For each $Y_n^m: n = 0,2,\ldots,N-1, m = 0,2,\ldots n$:

(7a) $$\sum_{k=1}^{3}\Big\{(\mathcal{L}_{xx}-\mathcal{L}_{yy})\big[(1+\delta_{m2})a_k^{nm} I_{n+4-2k}^{m-2} + e_k^{nm} I_{n+4-2k}^{m+2}\big] + (\mathcal{L}_{xy}+\mathcal{L}_{yx})\Big[-(1-\delta_{m2})a_k^{nm} I_{n+4-2k}^{-(m-2)} + e_k^{nm} I_{n+4-2k}^{-(m+2)}\Big] + (\mathcal{L}_{xx}+\mathcal{L}_{yy})c_k^{nm} I_{n+4-2k}^{m}\Big\} - (1-\omega\delta_{0n})I_n^m = -(1-\omega)I_b\delta_{0n}$$

and for each $Y_n^{-m}: n = 2,\ldots,N-1, m = 2,\ldots n$:

(7b) $$\sum_{k=1}^{3}\Big\{(\mathcal{L}_{xy}+\mathcal{L}_{yx})\big[(1+\delta_{m2})a_k^{nm} I_{n+4-2k}^{m-2} - e_k^{nm} I_{n+4-2k}^{m+2}\big] + (\mathcal{L}_{xx}-\mathcal{L}_{yy})\Big[(1-\delta_{m2})a_k^{nm} I_{n+4-2k}^{-(m-2)} + e_k^{nm} I_{n+4-2k}^{-(m+2)}\Big] + (\mathcal{L}_{xx}+\mathcal{L}_{yy})c_k^{nm} I_{n+4-2k}^{-m}\Big\} - I_n^{-m} = 0$$

where ω is the scattering albedo and is restricted to isotropic scattering here, a_k^{nm}, c_k^{nm} and e_k^{nm} are constant coefficients given in [3], [8], and δ_{ij} is the Kronecker delta function. The $\mathcal{L}$ operators are denoting the derivatives. For example,

(8) $$\mathcal{L}_{xy} = \frac{1}{\beta_r}\frac{\partial}{\partial x}\left(\frac{1}{\beta_r}\frac{\partial}{\partial y}\right)$$

The boundary conditions derived from the general Marshak's condition are usually expressed in local coordinates in terms of the surface normal and tangential vectors. The local coordinates can be set up as in Fig.

1, so that $\bar{I}_n^m$ is independent of $\bar{y}$ (pointing into the global z-direction). Meanwhile, the $\bar{x}$ direction can be found from Euler angles defined in [9], and Fig. 1 shows both the arrangements of the global and local coordinates for a general 2-D Cartesian geometry in the $x-y$ plane.

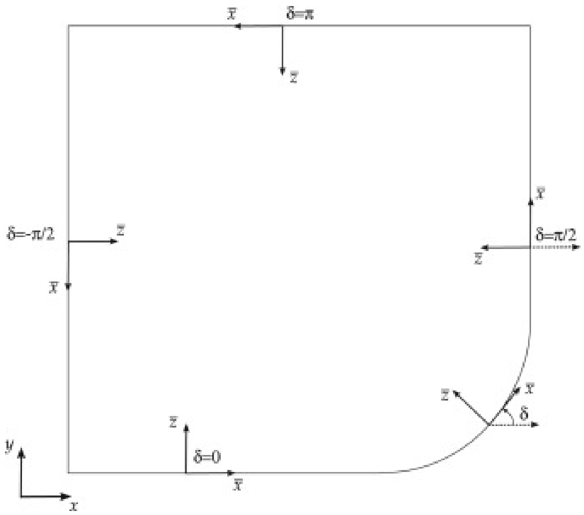

Fig. 1. Schematic of the global coordinate system and the local coordinate system in $x-y$ plane.

The Euler angles are calculated from [9]

(9a) $\alpha = \tan^{-1}\left(\frac{n_y}{n_x}\right) = \delta + \frac{\pi}{2}$

(9b) $\beta = \frac{\pi}{2}$

resulting in

(10a) $\hat{\mathbf{n}} = \cos\alpha\hat{\imath} + \sin\alpha\hat{\jmath} = -\sin\delta\hat{\imath} + \cos\delta\hat{\jmath}$

(10b) $\hat{\mathbf{t}}_{\bar{x}} = \sin\alpha\hat{\imath} - \cos\alpha\hat{\jmath} = \cos\delta\hat{\imath} + \sin\delta\hat{\jmath}$

Because of the two-dimensionality, we have $I(\bar{\theta},\bar{\psi}) = I(\bar{\theta},-\bar{\psi})$ with the local azimuthal angle $\bar{\psi}$ defined in the $\bar{x}-\bar{y}$ plane and measured from the local $\bar{x}-$ axis, which leads to the elimination of $\bar{I}_n^m$ with negative m. Together with the elimination of the I_n^m with odd m in global coordinates, the $(N+1)^2/4$ boundary conditions for 2-D problems become

For each Y¯2i−10, i=1,2,...,(N+1)/2:

(11a) $I_w p_{0,2i-1}^0 = \sum_{l=0}^{(N-1)/2}\sum_{m'=-l}^{l} p_{2l,2i-1}^0 \bar{\Delta}_{0,2m'}^{2l} I_{2l}^{2m'} + \frac{\partial}{\partial\tau_{\bar{x}}}\sum_{l=1}^{(N-1)/2}\sum_{m'=-l}^{l} v_{l,i}^0 \bar{\Delta}_{1,2m'}^{2l} I_{2l}^{2m'} - \frac{\partial}{\partial\tau_{\bar{z}}}\sum_{l=0}^{(N-1)/2}\sum_{m'=-l}^{l} w_{l,i}^0 \bar{\Delta}_{0,2m'}^{2l} I_{2l}^{2m'}$

and for each $\bar{Y}_{2i-1}^m$, $i = 1,2,\ldots,(N-1)/2, m = 1,2,\ldots,2i-1; i = (N+1)/2, m = 2,4,\ldots,2i-2$:

$$(11b)\ 0=\sum_{l=0}^{(N-1)/2}\sum_{m'=-l}^{l} p_{2l,2i-1}^{m}\bar{\Delta}_{\pm m,2m'}^{2l} I_{2l}^{2m'}-\frac{\partial}{\partial\bar{\tau}_x}\sum_{l=0}^{(N-1)/2}\sum_{m'=-l}^{l}\left[(1+\delta_{m,1})u_{l,i}^{m}\bar{\Delta}_{m-1,2m'}^{2l}-v_{l,i}^{m}\bar{\Delta}_{m+1,2m'}^{2l}\right]I_{2l}^{2m'}-\frac{\partial}{\partial\bar{\tau}_z}\sum_{l=0}^{(N-1)/2}\sum_{m'=-l}^{l} w_{l,i}^{m}\bar{\Delta}_{\pm m,2m'}^{2l} I_{2l}^{2m'}$$

where the constant coefficients $u_{l,i}^{m}$, $v_{l,i}^{m}$, $w_{l,i}^{m}$, and $p_{2l,n}^{m}$ can be found in [3], and $\bar{\Delta}_{m,m'}^{n}\left(\frac{\pi}{2},-\frac{\pi}{2},-\alpha\right)$ is the rotation matrix [3]. I_w is the radiative intensity at the boundary wall, which is determined from

$$(12)\ I_w=\epsilon I_{bw}+(1-\epsilon)\frac{H}{\pi}$$

where ϵ is the surface emittance, and H is the hemispherical irradiation. For black walls, $\epsilon=1$, this leads to $I_w=I_{bw}$. For clarity, here the definition of I_w, Eq. (12), is limited to diffusely reflecting walls. More explanation and further development for walls with more complicated properties will be presented in the special boundary condition section.

2.2. Implementation

The coupled $(N+1)^2/4$ simultaneous PDEs and their boundary conditions are solved iteratively by the finite volume based software *OpenFOAM*. In each PDE with n and m corresponding to $Y_n^{\pm m}$, the $I_n^{\pm m}$ and their derivatives are arranged to employ the finite volume Laplacian operator of *OpenFOAM*, i.e.,

$$(13)\ (\mathcal{L}_{xx}+\mathcal{L}_{yy})c_2^{nm}I_n^{\pm m}-(1-\omega\delta_{0n})I_n^{\pm m}=c_2^{nm}\nabla_\tau^2 I_n^{\pm m}-(1-\omega\delta_{0n})I_n^{\pm m}$$

All terms other than $I_n^{\pm m}$ are updated before each $I_n^{\pm m}$ iteration (before solving the corresponding $Y_n^{\pm m}$ governing equation). The preconditioned conjugate gradient (PCG) [10] algorithm is used to solve each PDE sequentially until I_0^0 has converged to prescribed criteria. For a 2-D problem on the $x-y$ plane, the iteration sequence can be optimized by iterating the I_n^0 terms first.

In order to implement the boundary conditions (11a), (11b), the system of $(N+1)^2/4$ boundary conditions is transformed to a matrix form, which then can generate one Robin-type boundary condition for each of the corresponding governing equations. The boundary conditions are rearranged into matrices and vectors in the same way as described in [4], where $\mathbf{p}$, $\mathbf{Q}$, $\mathbf{Q}_{\bar{x}}$ and $\mathbf{Q}_{\bar{z}}$ are coefficient matrices and $\mathbf{I}=[I_1,I_2,I_3,\ldots,I_j,\ldots]^T=[I_0^0,I_2^{-2},I_2^0,I_2^2,I_4^{-4},\ldots]^T$ is the vector of unknowns (intensity coefficients I_n^m):

$$(14)\ \mathbf{Q}\cdot\mathbf{I}+\mathbf{Q}_{\bar{x}}\cdot\frac{\partial\mathbf{I}}{\partial\bar{\tau}_x}+\mathbf{Q}_{\bar{z}}\cdot\frac{\partial\mathbf{I}}{\partial\bar{\tau}_z}=I_{bw}\mathbf{p}$$

Eq. (14) can be converted to $N_2=(N+1)^2/4$ Robin-type boundary conditions,

$$(15)\ I_j+Z_{j,j}\frac{\partial I_j}{\partial\bar{\tau}_z}=\delta_{j,1}I_{bw}-\sum_{k=1}^{N_2}\left[X_{j,k}\frac{\partial I_k}{\partial\bar{\tau}_x}+(1-\delta_{j,k})Z_{j,k}\frac{\partial I_k}{\partial\bar{\tau}_z}\right]$$

where $\mathbf{X}$, $\mathbf{Z}$ are defined as

$$(16)\ \mathbf{X}=\mathbf{Q}^{-1}\cdot\mathbf{Q}_{\bar{\mathbf{x}}},\ \mathbf{Z}=\mathbf{Q}^{-1}\cdot\mathbf{Q}_{\bar{\mathbf{z}}}$$

and are evaluated through LU decomposition [11] of $\mathbf{Q}$. A similar stabilizer as in [4] for the 3-D formulation is also defined for the 2-D P_N for optically thin simulations.

3. Special boundary conditions for P_N

3.1. Nonblack surfaces and mixed diffuse-specular reflecting surfaces

In this section, the general boundary condition for mixed diffuse-specular surfaces is derived, which then is readily reduced to simpler approximations, such as a diffuse or a specular surface.

For a partially diffuse and partially specular surface, the emissivity can be expressed as

(17) $\epsilon = 1 - \rho^s - \rho^d$

where ρ^s and ρ^d are the specular and diffuse components of the reflectance, respectively. The outgoing intensity I_w for partially diffuse and partially specular surfaces consists of two components: one part is due to the intensity from diffuse emission I_{bw} as well as the diffuse fraction of reflected energy H/π, while the other is the specular fraction of reflected energy I^s:

(18) $I_w = \epsilon I_{bw} + \rho^d \frac{H}{\pi} + \rho^s I^s$

The hemispherical irradiation H in the P_N context is evaluated by multiplying Eq. (1) by Y_1^0 (or $\cos\theta$) and integrating over the hemisphere, or

(19) $$H = \int_{\hat{\mathbf{n}}\cdot\hat{\mathbf{s}}<0} I Y_1^0 d\Omega = \sum_{n=0}^{N} \sum_{m=-n}^{n} \int_0^{2\pi} \int_{-1}^{0} I_n^m Y_n^m Y_1^0 d\mu d\psi = 2\pi \sum_{n=0}^{N} (-1)^n p_{n,1}^0 I_n^0$$

Substituting Eqs. (18), (19) into the general Marshak boundary condition (5), we have

(20) $$(1+\delta_{m,0})\pi \sum_{n=0}^{N} p_{n,2i-1}^m I_n^m = 2\pi \delta_{m,0} p_{0,2i-1}^0 [\epsilon I_{bw} + 2\rho^d \sum_{n=0}^{N} (-1)^n p_{n,1}^0 I_n^0] + \rho^s \int_0^{2\pi} \int_0^1 I^s Y_{2i-1}^m d\mu d\psi$$

I^s can be found by the law of specular reflection, which is

(21) $$I^s(\theta,\psi) = I(\pi-\theta,\psi) = \sum_{n=0}^{N} \sum_{m=-n}^{n} I_n^m Y_n^m(\pi-\theta,\psi) = \sum_{n=0}^{N} \sum_{m=-n}^{n} I_n^m Y_n^m(-\mu,\psi)$$

The associated Legendre polynomials, given by Eq. (3), are even functions when $(m+n)$ are even and odd functions when $(m+n)$ are odd, which leads to

(22) $$I^s = \sum_{n=0}^{N} \sum_{m=-n}^{n} (-1)^{(m+n)} I_n^m Y_n^m(\mu,\psi)$$

Therefore, Eq. (20) becomes

(23) $$\sum_{n=0}^{N}\left\{\left[1-(-1)^{m+n}\underbrace{\rho^{s}}_{\text{(a)specularreflection}}\right]p_{n,2i-1}^{m}-2(-1)^{n}\delta_{m,0}\underbrace{\rho^{d}}_{\text{(b)diffusereflection}}p_{0,2i-1}^{0}p_{n,1}^{0}\right\}\bar{I}_{n}^{m}=\delta_{m,0}p_{0,2i-1}^{0}\underbrace{\epsilon I_{bw}}_{\text{(c)emission}}\quad i=1,2,\dots,\tfrac{1}{2}(N+1),\ \text{all relevant } m$$

Following [3], all m are employed for $i=1,2,3,\dots,(N-1)/2$ and only even m are employed for $i=(N+1)/2$. When $\epsilon=1$, $\rho^{s}=0$ and $\rho^{d}=0$, Eq. (23) is simply the original Marshak boundary condition for black walls [1], [2] as expected; when $\rho^{s}=1$ or $\rho^{d}=1$, Eq. (23) gives the boundary conditions for the purely specular or purely diffuse surfaces, respectively; when $N=1$, there is no distinction between diffuse and specular surface reflectivities for P_1 approximation, which is consistent with the conclusion obtained in [12].

Before Eq. (23) can be applied to the elliptical formulation described in this paper, the $\bar{I}_{n}^{m}$ with odd n need to be eliminated and the local $\bar{I}_{n}^{m}$ need to be rotated back to global I_{n}^{m}. Expanding part (b) of Eq. (23), we get

(24) $$-2p_{0,2i-1}^{0}\rho^{d}\sum_{n=0}^{N}(-1)^{n}p_{n,1}^{0}\bar{I}_{n}^{0}=-2p_{0,2i-1}^{0}\rho^{d}\left[\left(p_{0,1}^{0}\bar{I}_{0}^{0}+p_{2,1}^{0}\bar{I}_{2}^{0}+p_{4,1}^{0}\bar{I}_{4}^{0}+p_{6,1}^{0}\bar{I}_{6}^{0}+\cdots\right)-p_{1,1}^{0}\bar{I}_{1}^{0}\right]$$

Since $p_{n,j}^{m}\equiv 0$ when $n+j$ is even and $n\neq j$ [3], $p_{n,1}^{0}=0$ when n is odd and $n\neq 1$. When $n=1$, $\bar{I}_{1}^{0}$ is calculated as [3]

(25) $$\bar{I}_{1}^{0}=-\frac{\partial\bar{I}_{0}}{\partial\bar{\tau}_{z}}-\frac{2}{5}\frac{\partial\bar{I}_{2}^{0}}{\partial\bar{\tau}_{z}}+\frac{3}{5}\frac{\partial\bar{I}_{2}^{1}}{\partial\bar{\tau}_{x}}+\frac{3}{5}\frac{\partial\bar{I}_{2}^{-1}}{\partial\bar{\tau}_{y}}$$

in terms of local $\bar{I}_{n}^{m}$. The local intensity coefficients $\bar{I}_{n}^{m}$ in Eq. (25) are then rotated back to global I_{n}^{m} through the rotation function,

(26) $$\bar{I}_{n}^{m}=\sum_{m'=-n}^{n}\bar{\Delta}_{mm'}^{n}I_{n}^{m'}$$

which are

(27a) $$\bar{I}_{2}^{0}=\bar{\Delta}_{0,-2}^{2}I_{2}^{-2}+\bar{\Delta}_{0,-1}^{2}I_{2}^{-1}+\bar{\Delta}_{0,0}^{2}I_{2}^{0}+\bar{\Delta}_{0,1}^{2}I_{2}^{1}+\bar{\Delta}_{0,2}^{2}I_{2}^{2}$$

(27b) $$\bar{I}_{2}^{1}=\bar{\Delta}_{1,-2}^{2}I_{2}^{-2}+\bar{\Delta}_{1,-1}^{2}I_{2}^{-1}+\bar{\Delta}_{1,0}^{2}I_{2}^{0}+\bar{\Delta}_{1,1}^{2}I_{2}^{1}+\bar{\Delta}_{1,2}^{2}I_{2}^{2}$$

(27c) $$\bar{I}_{2}^{-1}=\bar{\Delta}_{-1,-2}^{2}I_{2}^{-2}+\bar{\Delta}_{-1,-1}^{2}I_{2}^{-1}+\bar{\Delta}_{-1,0}^{2}I_{2}^{0}+\bar{\Delta}_{-1,1}^{2}I_{2}^{1}+\bar{\Delta}_{-1,2}^{2}I_{2}^{2}$$

For Cartesian coordinates, the rotation matrices $\bar{\Delta}_{m,m'}^{n}$ are fixed values for a given boundary location and thus are not affected by the differentiation in Eq. (25). Similarly, the other $\bar{I}_{n}^{0}$ with even n in Eq. (24) are also rotated back to global I_{n}^{m} through Eq. (26). Physically, $\bar{I}_{1}^{0}$ gives the normal heat flux at the wall,

(28) $$\mathbf{q}\cdot\hat{\mathbf{n}}=q_{w}=\frac{4\pi}{3}\bar{I}_{1}^{0}$$

It is seen that part (b) of Eq. (23) only requires the $\bar{I}_n^0$ for local spherical harmonics $\bar{Y}_n^0$ and the heat flux at the wall, q_w, while the specular reflection, part (a) of Eq. (23), requires of all the $\bar{I}_n^m$.

The specular reflection, part (a) of Eq. (24), adds no extra terms but changes the coefficients of $\bar{I}_n^m$. Comparing Eq. (24) with Eq. (6), we find it convenient to define

(29) $\hat{p}_{n,2i-1}^m = [1-(-1)^{m+n}\rho^s]p_{n,2i-1}^m - 2\delta_{m,0}\rho^d p_{0,2i-1}^0 p_{n,1}^0$

and the coefficients $\hat{u}_{l,i}^m$, $\hat{v}_{l,i}^m$ and $\hat{w}_{l,i}^m$ as

(30a) $\hat{u}_{l,i}^m = [1+(-1)^{(m+l)}\rho^s]u_{l,i}^m$

(30b) $\hat{v}_{l,i}^m = [1+(-1)^{(m+l)}\rho^s]v_{l,i}^m + \frac{2}{5}\delta_{m,0}\delta_{l,1}\rho^d p_{0,2i-1}^0$

(30c) $\hat{w}_{l,i}^m = [1+(-1)^{(m+l)}\rho^s]w_{l,i}^m + \frac{2}{3}\delta_{m,0}(\delta_{l,0}+\frac{2}{5}\delta_{l,1})\rho^d p_{0,2i-1}^0$

With these abbreviations and following the derivation in [2], [1], i.e., to express the $\bar{I}_n^m$ with odd n in terms of the derivatives of $\bar{I}_n^m$ with even n, and then rotating $\bar{I}_n^m$ back to global coordinates, Eq. (23) is converted into $N(N+1)/2$ boundary conditions for mixed diffuse-specular surfaces:

For each $\bar{Y}_{2i-1}^m$, $i = 1,2,\dots,(N+1)/2$,

$m = 0$:

$$(31a)\ 0 = \sum_{l=0}^{\frac{N-1}{2}}\sum_{m'=-2l}^{2l}\hat{p}_{2l,2i-1}^m \bar{\Delta}_{\pm m,m'}^{2l} I_{2l}^{m'} - \frac{\partial}{\partial\bar{\tau}_x}\sum_{l=l'}^{\frac{N-1}{2}}\sum_{m'=-2l}^{2l}[(1\pm\delta_{m,1})\hat{u}_{l,i}^m\bar{\Delta}_{\pm(m-1),m'}^{2l} - \hat{v}_{l,i}^m\bar{\Delta}_{\pm(m+1),m'}^{2l}]I_{2l}m' \pm \frac{\partial}{\partial\bar{\tau}_y}\sum_{l=1-l'}^{\frac{N-1}{2}}\sum_{m'=-2l}^{2l}[(1\mp\delta_{m,1})\hat{u}_{l,i}^m\bar{\Delta}_{\mp(m-1),m'}^{2l} + \hat{v}_{l,i}^m\bar{\Delta}_{\mp(m+1),m'}^{2l}]I_{2l}^{m'} - \frac{\partial}{\partial\bar{\tau}_z}\sum_{l=0}^{\frac{N-1}{2}}\sum_{m'=-2l}^{2l}\hat{w}_{l,i}^m\bar{\Delta}_{\pm m,m'}^{2l} I_{2l}^{m'}$$

where we define l' as

$$(32)\ l' = \begin{cases} 0 & \text{for} \bar{Y}_{2i-1}^m \\ 1 & \text{for} \bar{Y}_{2i-1}^{-m} \end{cases}$$

and again, for $i = (N+1)/2$ only even m are employed [3]. The form of Eq. (31a), (31b) is identical to the boundary conditions for black walls developed in [4]. The newly defined coefficients $\hat{p}_{n,2i-1}^m$, $\hat{u}_{l,i}^m$, $\hat{v}_{l,i}^m$ and $\hat{w}_{l,i}^m$ are readily integrated into the matrix formulation [4] by adding the coefficients to the corresponding rows of the original matrices $\mathbf{Q}$, $\mathbf{Q}_{\bar{x}}$, $\mathbf{Q}_{\bar{y}}$ and $\mathbf{Q}_{\bar{z}}$.

Following the 2-D formulation in this paper, Eqs. (31a), (31b) can also be applied to 2-D problems by eliminating the I_n^m with odd m in global coordinates and the $\bar{I}_n^m$ with negative m in the local coordinates. This leads to

(33a) $\bar{I}_2^0 = \bar{\Delta}_{0,-2}^2 \bar{I}_2^{-2} + \bar{\Delta}_{0,0}^2 I_2^0 + \bar{\Delta}_{0,2}^2 I_2^2$

(33b) $\bar{I}_2^1 = \bar{\Delta}_{1,-2}^2 \bar{I}_2^{-2} + \bar{\Delta}_{1,0}^2 I_2^0 + \bar{\Delta}_{1,2}^2 I_2^2$

Then Eqs. (31a), (31b) reduce to

For each $\bar{Y}_{2i-1}^m$, $i = 1,2, \dots, (N+1)/2$:

$m \neq 0$:

$$(34a)\ 0 = \sum_{l=0}^{\frac{N-1}{2}} \sum_{m'=-l}^{l} \hat{p}_{2l,2i-1}^{m} \bar{\Delta}_{\pm m,2m'}^{2l} I_{2l}^{2m'} - \frac{\partial}{\partial \bar{\tau}_x} \sum_{l=0}^{\frac{N-1}{2}} \sum_{m'=-l}^{l} [(1 \pm \delta_{m,1}) \hat{u}_{l,i}^{m} \bar{\Delta}_{\pm(m-1),m'}^{2l} - \hat{v}_{l,i}^{m} \bar{\Delta}_{\pm(m+1),2m'}^{2l}]\, I_{2l}^{2m'} - \frac{\partial}{\partial \bar{\tau}_z} \sum_{l=0}^{\frac{N-1}{2}} \sum_{m'=-l}^{l} \hat{w}_{l,i}^{m} \bar{\Delta}_{\pm m,2m'}^{2l} I_{2l}^{2m'}$$

the form of Eqs. (34a), (34b) is identical to the boundary conditions (11a), (11b) for black walls except for the new definitions of coefficients.

3.2. Specified radiative flux at the wall

The Marshak boundary conditions in the 3-D formulation [4] were transformed to Robin type boundary conditions as

$$(35)\ I_j + Z_{j,j} \frac{\partial I_j}{\partial \bar{\tau}_z} = \delta_{j,1} I_w - \sum_{k=1}^{N_2} \left[X_{j,k} \frac{\partial I_k}{\partial \bar{\tau}_x} + Y_{j,k} \frac{\partial I_k}{\partial \bar{\tau}_y} + (1 - \delta_{j,k}) Z_{j,k} \frac{\partial I_k}{\partial \bar{\tau}_z} \right]$$

Note that only the boundary condition for $j = 1$ (with $I_1 = I_0^0$) includes the radiative intensity I_w from the wall. Based on the relation between the radiative flux and local intensity coefficients [3], the specified radiative wall flux condition is implemented by replacing the equation for I_1 with Eq. (28), where the $\bar{I}_1^0$ is given by Eq. (25). For a given q_w, this leads to a boundary condition of the second type,

$$(36)\ \frac{\partial \bar{I}_0}{\partial \bar{\tau}_z} = -\frac{2}{5} \frac{\partial \bar{I}_2^0}{\partial \bar{\tau}_z} + \frac{3}{5} \frac{\partial \bar{I}_2^1}{\partial \bar{\tau}_x} + \frac{3}{5} \frac{\partial \bar{I}_2^{-1}}{\partial \bar{\tau}_y} - \frac{3}{4\pi} q_w$$

if $q_w = 0$ (insulated boundary),

$$(37)\ \frac{\partial \bar{I}_0}{\partial \bar{\tau}_z} = -\frac{2}{5} \frac{\partial \bar{I}_2^0}{\partial \bar{\tau}_z} + \frac{3}{5} \frac{\partial \bar{I}_2^1}{\partial \bar{\tau}_x} + \frac{3}{5} \frac{\partial \bar{I}_2^{-1}}{\partial \bar{\tau}_y}$$

Again, the local intensity coefficients $\bar{I}_n^m$ in Eq. (37) are rotated back to global I_n^m through the rotation function (26), which expands to Eq. (27a), (27b), (27c) for the 3-D formulation and Eqs. (33a), (33b) for the 2-D formulation.

3.3. Symmetry/specular reflection boundary condition

At a symmetry/specular reflection boundary, the local polar angle $\bar{\theta}$ is measured from the local $\bar{z} -$ axis, and therefore

(38) $\bar{I}\left(\bar{\theta},\bar{\psi}\right) = \bar{I}\left(\pi - \bar{\theta},\bar{\psi}\right)$

Eq. (3) shows the odd-power dependence on $\cos\bar{\theta}$ when n+m is odd, thus all $\bar{I}_n^m = 0$ when $n + m$ is odd, which provides the required $N(N + 1)/2$ boundary conditions. However, since only I_n^m with even n are solved for, $\bar{I}_n^m$ with odd n must be expressed in terms of $\bar{I}_{n+1}^m$ and $\bar{I}_{n-1}^m$.

Applying the relationship between $\bar{I}_n^m$, $\bar{I}_{n+1}^m$ and $\bar{I}_{n-1}^m$ [2], while connecting the global I_n^m with the local $\bar{I}_n^m$ through the rotation function Eq. (26), the $N(N + 1)/2$ boundary conditions are found as:

For all even $n = 0,2, \ldots, N - 1$,

when m is even:

(39a) $\frac{\partial \bar{I}_n^m}{\partial \tau_{\bar{z}}} = \frac{\partial}{\partial \tau_{\bar{z}}} \sum_{m'=-n}^{n} \bar{\Delta}_{m,m'}^n I_n^{m'} = 0$

when m is odd:

(39b) $\bar{I}_n^m = \sum_{m'=-n}^{n} \bar{\Delta}_{m,m'}^n I_n^{m'} = 0$

For the case of $\bar{I}_0^0 = I_0^0$, Eq. (39a) is a boundary condition of the second type, which can be applied directly. For the remainder of the boundary conditions, the variables I_n^m and their surface normal derivatives, $\partial I_n^m/\partial \tau_{\bar{z}}$, are coupled through the summation terms in Eqs. (39a), (39b). These boundary conditions are difficult to apply directly for the segregated iterations of the governing equations of P_N. In *OpenFOAM* (and other finite volume based CFD programs with unstructured grids), the surface normal derivatives are discretized as

(40) $\frac{\partial \mathbf{I}}{\partial \tau_{\bar{z}}} = \frac{\mathbf{I}'_{cell,\mathbf{n}} - \mathbf{I}_{wall}}{\beta_{r,cell}|\mathbf{n}|}$

is the vector $\mathbf{d}$ is the distance vector from the face center to the neighboring cell center; $\mathbf{I}'_{cell,\mathbf{n}}$ is found by using the old value of $\nabla \mathbf{I}_{cell}$ from the previous iteration at the cell (deferred correction) as

(42) $\mathbf{I}'_{cell,\mathbf{n}} = \mathbf{I}_{cell} + (\nabla \mathbf{I}_{cell})_{old} \cdot \mathbf{k}$

For orthogonal meshes (where the surface normals pass through the cell centers of the neighboring cell, or $\mathbf{d} = \mathbf{n}$), Eq. (40) becomes

(44) $\frac{\partial \mathbf{I}}{\partial \tau_{\bar{z}}} = \frac{\mathbf{I}_{cell} - \mathbf{I}_{wall}}{\beta_{r,cell}|\mathbf{d}|}$

Taking P_3 as an example, the corresponding five boundary conditions resulting from Eqs. (39a), (39b) become

(45) $$\begin{bmatrix} \frac{\bar{\Delta}^2_{-2,-2}}{\beta_r|\mathbf{n}|} & \cdots & \cdots & \frac{\bar{\Delta}^2_{-2,2}}{\beta_r|\mathbf{n}|} \\ \bar{\Delta}^2_{-1,-2} & \cdots & \cdots & \bar{\Delta}^2_{-1,2} \\ \frac{\bar{\Delta}^2_{0,-2}}{\beta_r|\mathbf{n}|} & \cdots & \cdots & \frac{\bar{\Delta}^2_{0,2}}{\beta_r|\mathbf{n}|} \\ \bar{\Delta}^2_{1,-2} & \cdots & \cdots & \bar{\Delta}^2_{1,2} \\ \frac{\bar{\Delta}^2_{2,-2}}{\beta_r|\mathbf{n}|} & \cdots & \cdots & \frac{\bar{\Delta}^2_{2,2}}{\beta_r|\mathbf{n}|} \end{bmatrix} \begin{bmatrix} I_2^{-2} \\ I_2^{-1} \\ I_2^{0} \\ I_2^{1} \\ I_2^{2} \end{bmatrix}_{wall} = \begin{bmatrix} \frac{\bar{\Delta}^2_{-2,-2}}{\beta_r|\mathbf{n}|} & \cdots & \cdots & \frac{\bar{\Delta}^2_{-2,2}}{\beta_r|\mathbf{n}|} \\ 0 & \cdots & \cdots & 0 \\ \frac{\bar{\Delta}^2_{0,-2}}{\beta_r|\mathbf{n}|} & \cdots & \cdots & \frac{\bar{\Delta}^2_{0,2}}{\beta_r|\mathbf{n}|} \\ 0 & \cdots & \cdots & 0 \\ \frac{\bar{\Delta}^2_{2,-2}}{\beta_r|\mathbf{n}|} & \cdots & \cdots & \frac{\bar{\Delta}^2_{2,2}}{\beta_r|\mathbf{n}|} \end{bmatrix} \begin{bmatrix} I_2^{-2} \\ I_2^{-1} \\ I_2^{0} \\ I_2^{1} \\ I_2^{2} \end{bmatrix}_{cell}$$

Here we denote the coefficient matrix on the left-hand side as $\mathbf{A}$, and the matrix on the right-hand side as $\mathbf{B}$. Note that the rows of $\mathbf{A}$ and $\mathbf{B}$ can be in any order, while the order of the columns should be correctly related to the I_n^m. After each iteration, the I_n^m at boundary walls can be calculated from

(46) $\mathbf{I}_{wall} = \mathbf{A}^{-1}\mathbf{B}\mathbf{I}'_{cell,\mathbf{n}}$

or

(47) $\mathbf{I}_{wall} = \mathbf{A}^{-1}\mathbf{B}\mathbf{I}_{cell}$

in the case of orthogonal meshes. The 2-D formulation can be simplified from the 3-D formulation by eliminating the I_n^m with odd m in global coordinates and the $\bar{I}_n^m$ with negative m in local coordinates, which has been illustrated by Eqs. (27a), (27b), (27c), (33a), (33b). It is worth mentioning that the above derivation is not based on Marshak boundary condition, while it gives the same boundary conditions as Eq. (31a), (31b) for purely specular surfaces ($\rho_s = 1$).

4. Results and discussion

The 2-D Cartesian formulation of high-order spherical harmonic methods and the special boundary conditions are tested for three example cases with strongly varying temperatures and absorption coefficients. Although isotropic scattering adds no additional complexity or effort to P_N (as opposed to DOM), all the examples are limited to nonscattering media in this study simply to reduce parameters needed for presentation.

4.1. Square enclosure with variable radiative properties

The first example is two-dimensional radiative transfer in a square enclosure of a gray medium with variable radiative properties, which has been reported in [4]. The 2-D Cartesian P_N solver up to order 7 as well as the 3-D P_N solver are tested and compared against PMC results. A 51×51×1 cube is employed, and the properties of the medium vary according to

(48a) $I_b = 1 + 5r^2(2 - r^2)$

(48b) $\kappa = C_k[1 + 3.75(2 - r^2)^2]$

(48c) $r^2 = x^2 + y^2, -1 \le x \le 1, -1 \le y \le 1$

(48d) $\tau_D = 18\sqrt{2}C_k$

The symmetry/specular reflection boundary conditions are implemented for the walls at the suppressed dimension (z-direction for this case), and the other walls are black and cold. The results of incident radiation G and radiative heat source $-\nabla \cdot \mathbf{q}$ are shown in Fig. 2, comparing results from 2-D P_1 to P_7 with those of a 3-D solver and a Monte Carlo simulation.

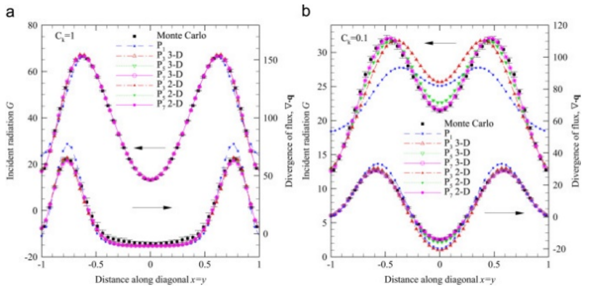

Fig. 2. Incident radiation and radiative heat source from a 2-D Cartesian P_N solver, a 3-D P_N solver and a *PMC* solver for a square enclosure. (a) *C*$_k$=1 (optically thick) and (b) *C*$_k$=0.1 (optically intermediate).

The results show that the 2-D Cartesian P_N solvers are indistinguishable from the 3-D results using fewer PDEs and unknowns. Also, results from the 3-D P_N solver with the new symmetry/specular reflection boundary conditions are identical to the results given by [4]. In the *OpenFOAM* finite volume implementation presented in [4], the 2-D square case is solved by treating walls of a 3-D cube at $z = const.$ as symmetry planes, which sets the normal gradients at the wall to zero for all scalars. While such implementation satisfies Eq. (39a), (39b) because the I_n^m of odd m for a 2-D case in the $x-y$ plane are zero everywhere, this is not true for general cases, where the symmetry/specular reflection boundary conditions need to be employed.

Fig. 3 shows the radiative flux q_w along one of the cold black walls. To test the specified-q_w boundary condition, one wall in each direction (x and y) is flagged as a specified-q_w boundary condition by inputting q_w according to the profile shown in Fig. 3 (first obtained by setting all walls to cold and black), while the opposite walls are kept as black and cold. Both 2-D Cartesian P_N and 3-D P_N with specified-q_w boundary conditions were tested and results were almost identical to the results shown in Fig. 2. Fig. 4 shows the contour plot of $-\nabla \cdot \mathbf{q}$ from the 2-D Cartesian *P*$_7$ solver with the specified-q_w boundary condition for the optically thick (*C*$_k$=1.0) case. The differences between the cases with and without the specified-q_w boundary condition are within 0.1%.

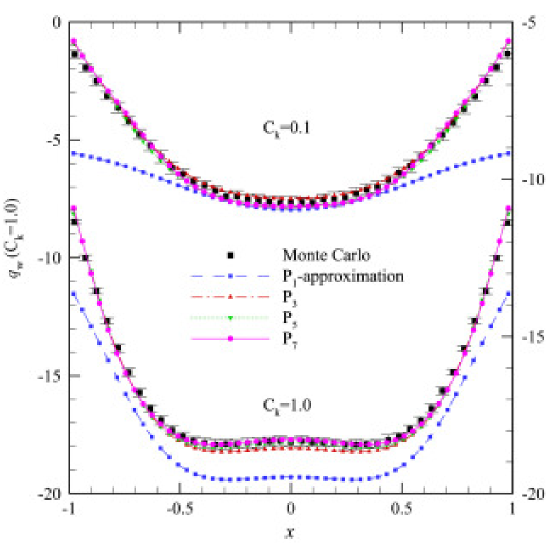

Fig. 3. Radiative flux q_w along the wall for *C*$_k$=0.1 and *C*$_k$=1.

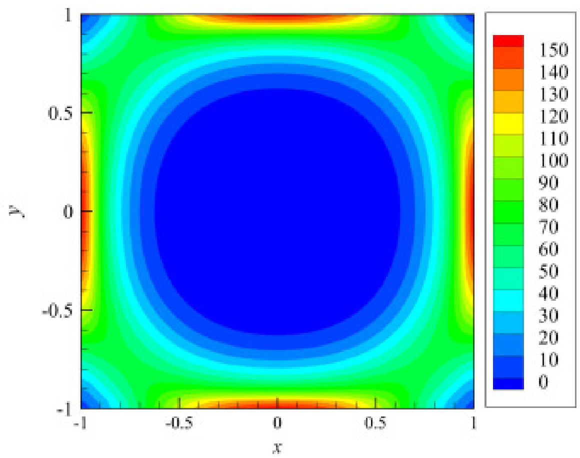

Fig. 4. The radiative heat source $-\nabla \cdot \mathbf{q}$ from 2-D Cartesian P_7 solver with specified-q_w boundary condition for the C_k=1.0 example. The upper wall ($y = 1$) and right wall ($x = 1$) employ specified-q_w boundary condition, while the other two are kept as black and cold wall.

This square enclosure example verifies the consistency and accuracy of the 2-D Cartesian P_N solver, the symmetry/specular reflection boundary condition and the specified radiative flux at the wall boundary condition.

4.2. Cylindrical enclosure and a 45° wedge enclosure

In the next example, the 2-D Cartesian P_N solver is further applied to a cylinder and a 45° wedge with the symmetry/specular reflection boundary condition. Many combustion problems in a cylindrical domain, such as in a Diesel engine (with multiple injectors along a circle), are periodically axisymmetric, in which the pattern of the azimuthal-angle-dependent flow field is repeated for every certain number of degrees. In these cases generally a wedge mesh instead of a full cylinder is chosen to expedite the simulation. To test the performance of the 2-D Cartesian high-order P_N methods (with r and ϕ expressed in terms of x and y) and the symmetry/specular reflection boundary condition for such meshes, simulations are carried out on a 45° wedge and a full cylinder (Fig. 5) with specified absorption coefficients κ and blackbody intensity I_b:

(49a) $I_b = 1 + \frac{20}{R^4} r^2 (R^2 - r^2)$

(49b) $\kappa = \left[1 + \frac{15}{R^4}(R^2 - r^2)^2\right]\left(1 + 0.5\frac{r}{R}\cos 8\phi\right)$

(49c) $0 \le r \le R = 0.5$

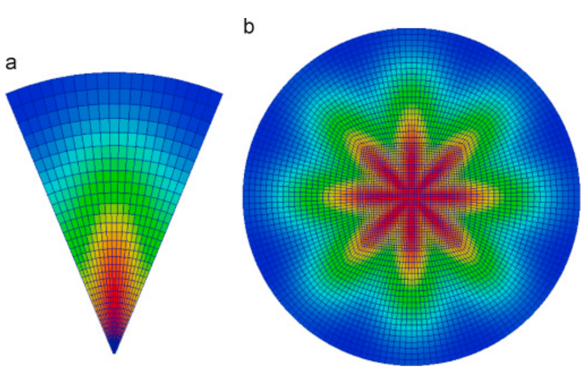

Fig. 5. The mesh of the 45° wedge (a) and the cylinder (b) in the analysis, the contour plot shows the κ distribution according to Eq. (49a), (49b), (49c).

The wedge has 45 cells along the radius and 21 cells in the circumferential direction with the tip cut off to avoid stability issues; the cylinder contains 20 cells along the radius with a square (41×41) at the center. The peripheral walls of the cylinder as well as the outer peripheral walls of the wedge are set to black and cold, while the flat walls of the wedge, the inner peripheral walls (cut-off tip) and the top and bottom of the cylinder are set to symmetry/specular reflection boundary condition.

The comparison of incident radiation, G, and radiative heat source, $-\nabla \cdot \mathbf{q}$, from P_1 to P_7 are shown in Fig. 6 for both meshes along the radius (at 0°). The P_N results from the 45° wedge mesh (lines with hollow symbols) overlap the results from the full cylinder (lines with solid symbol) at this position. Fig. 7 shows the contour plot of $-\nabla \cdot \mathbf{q}$ for P_7 from the 45° wedge. It is observed that the P_7 solutions from the 45° wedge match those from the cylinder (the differences are within 2% and mainly due to the grids), and similar comparisons were made for other orders of P_N methods and the results are consistent. The results of P_7 are very close to that of the PMC except at the cylinder/wedge center and at $r = 0.35$ as shown in Fig. 6b. The larger uncertainties of PMC close to the cylinder center are due to the sudden changes of the sizes of the cells at the cylinder center, and the discrepancy of P_7 at $r = 0.35$ maybe due to its remaining approximations, or due to inaccuracies in the PMC method (a zeroth order method, assuming properties to be constant across cells).

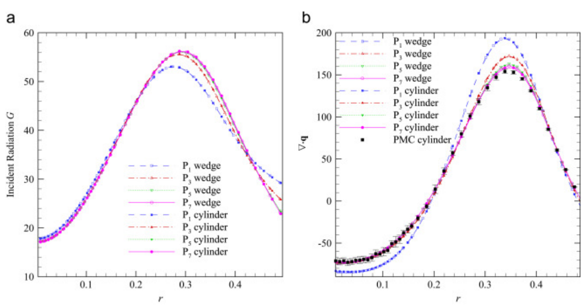

Fig. 6. Incident radiation G and radiative heat source $-\nabla \cdot \mathbf{q}$ along the centerline of a 45° wedge enclosure and that of a cylinder. (a) Incident radiation G and (b) radiative heat source $-\nabla \cdot \mathbf{q}$.

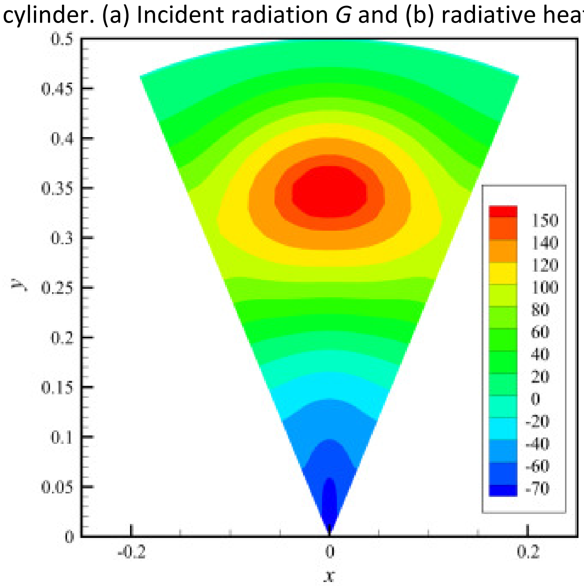

Fig. 7. The contour plot of radiative heat source $-\nabla \cdot \mathbf{q}$ from 2-D Cartesian P_7 solver for the 45° wedge.

4.3. Rectangular enclosure with mixed diffuse-specular gray walls

Polished metals and glassy materials, which display strong specular reflection peaks, can effectively be approximated by a combination of diffuse reflection and specular reflection. Sample simulations to test the accuracy of the high-order P_N method for mixed diffuse-specular walls have been performed on a 2-D rectangular geometry enclosed by walls with different surface characteristics. The geometry and radiative properties are shown in Fig. 8, and the properties of the left and right walls make up four test cases, i.e., (1) purely specular reflection ($\rho^s = 1$), (2) purely diffuse reflection ($\rho^d = 1$), (3) mixed diffuse-specular reflection without emission ($\epsilon = 0$, $\rho^s = 0.7$, $\rho^d = 0.3$) and (4) mixed diffuse-specular reflection with emission ($\epsilon = 0.5$, $\rho^s = 0.2$, $\rho^d = 0.3$).

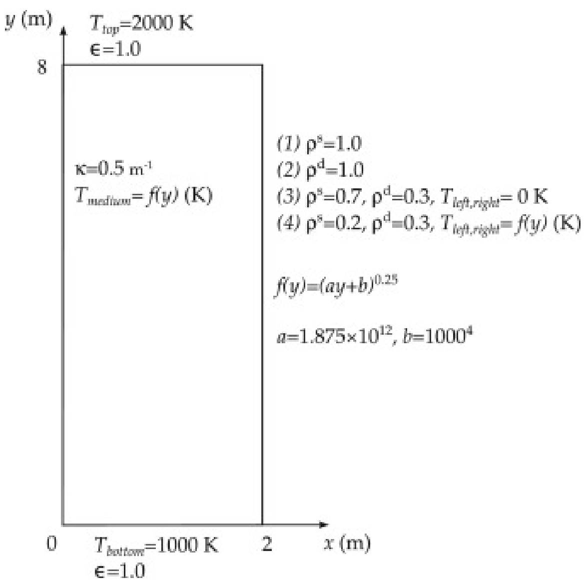

Fig. 8. Schematic of rectangular enclosure for tests of specular, diffuse and mixed diffuse-specular surfaces.

The radiative heat source, $\nabla \cdot \mathbf{q}$ along $x = 1$ m, and the heat flux at the wall, q_w, calculated with different orders of P_N as well as PMC are shown in Fig. 9, Fig. 10, Fig. 11 for Cases 2–4. Good agreement is observed between the results from high-order P_N and those from PMC for all three cases, where results for heat flux at the corners show the biggest discrepancies.

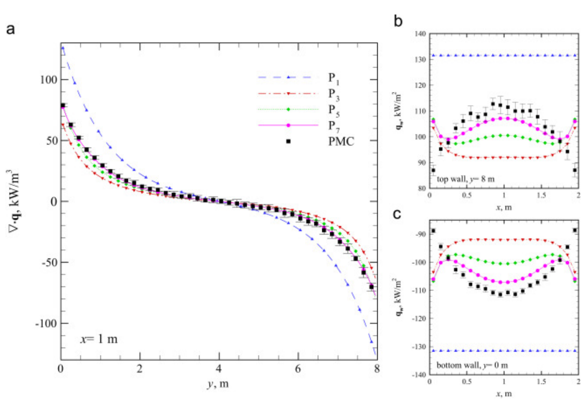

Fig. 9. Radiative heat source ∇·q along x=1 m and the heat flux q_w at top and bottom walls for Case 2. (a) x=1 m, (b) y=8 m and (c) y=0 m.

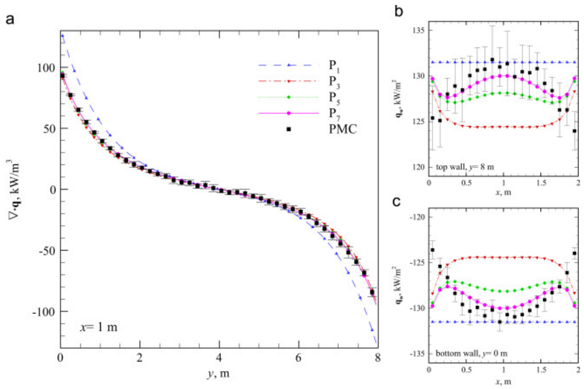

Fig. 10. Radiative heat source $\nabla \cdot \mathbf{q}$ along $x = 1$ m and the heat flux q_w at top and bottom walls for Case 3. (a) $x = 1$ m, (b) $y = 8$ m and (c) $y = 0$ m.

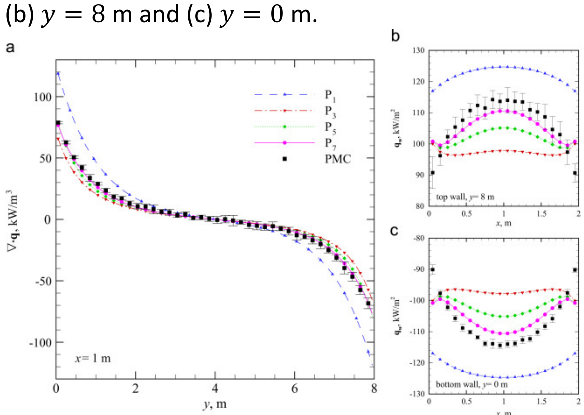

Fig. 11. Radiative heat source $\nabla \cdot q$ along $x = 1$ m and the heat flux q_w at top and bottom walls for Case 4. (a) $x = 1$ m, (b) $y = 8$ m and (c) $y = 0$ m.

Fig. 12 shows a comparison of the P_7 results for four surface characteristics. The differences between the results from Case 1 and Case 2 show that the wall properties can significantly affect the radiative heat source distributions and the heat flux profiles at the wall especially for larger aspect ratios. The differences between the results from purely diffuse walls and purely specular walls are expected to increase with higher aspect ratio of the geometry. Also, it is expected that the radiative heat source in the medium and the heat flux at walls for Case 3 lie between that of Case 1 and Case 2. These examples show that higher-order P_N methods are capable of solving problems with special surface properties, and the errors are acceptable when comparing to PMC results.

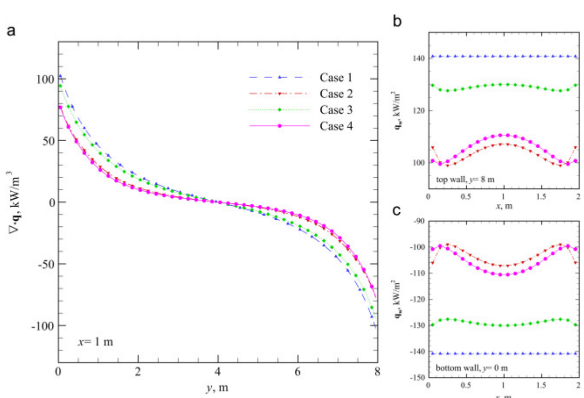

Fig. 12. Comparison of radiative heat source $\nabla \cdot \mathbf{q}$ and the heat flux at the wall q_w from P_7 solver for four surface properties.

4.4. Computation time comparison

A CPU time comparison for different orders of P_N for the above cases is given in Table 1. All calculations were carried out on a single Intel (R) Xeon (R) CPU X7460 running at 2.66 GHz. For the 2-D Cartesian formulation, P_3, P_5 and P_7 consist of 4, 9 and 16 strongly coupled PDEs with numerous cross-derivatives, respectively, while CPU time increases over P_1 are of the order of 60, 120 and 250, respectively. This nonlinear increase is due to the fact that the *OpenFOAM* implementation has not been optimized to solve simultaneous PDEs. The computation time for the 2-D Cartesian P_N solver is about 24%, 29% and 31% less than the time needed for 3-D P_3, P_5 and P_7, respectively. For the 45° wedge case, CPU time was found to be around 16% of that for the full cylinder, while the cell numbers of the 45° wedge are 19% of that of the cylinder. For the rectangular enclosure, the time costs for the four sets of different surface properties are almost the same. It is worth noting that the time cost is strongly related to the structure of the mesh and radiative properties through the number of iterations required. For CFD coupled computations, the mesh should be optimized for both the CFD calculations and the radiative transfer evaluation by the P_N method.

Table 1. Comparison of P_N computation cost for different test cases.

Solver	**Test case**	**Number of cells**	P_1**(s)**	P_3**(s)**	P_5**(s)**	P_7**(s)**
3-D	Square (C_k=1)	2601	0.02	0.75	4.71	7.00
2-D	Square (C_k=1)	2601	0.02	0.57	3.35	4.83
3-D	Square (C_k=0.1)	2601	0.02	0.87	5.05	9.33
2-D	Square (C_k=0.1)	2601	0.02	0.66	3.61	6.45
2-D	45° wedge	945	0.01	0.56	1.35	2.57
2-D	Cylinder	4961	0.06	3.59	8.72	16.61
2-D	Rectangle	1600	0.02	0.35	2.05	4.37

5. Summary and conclusion

A 2-D Cartesian version of the spherical harmonics P_N model (up to P_7) was extracted from the general 3-D P_N formulation and implemented in *OpenFOAM*. The number of PDEs and intensity coefficients for the 2-D Cartesian P_N was reduced from $N(N+1)/2$ to $(N+1)^2/4$. In addition, the Marshak boundary conditions for nonblack surfaces and mixed diffuse-specular surfaces were derived and boundary conditions for specified wall fluxes, for symmetry/specular reflection boundaries, were developed. A square enclosure, a 45° wedge, a full cylinder and a rectangular enclosure were tested for the 2-D Cartesian P_N formulation and the new boundary conditions. The correctness and accuracy of the new formulation and special boundary conditions were verified by comparing computations to intensity coefficients from the 3-D P_N formulation and with PMC results. The comparison shows that the 2-D formulation provides an accurate and faster approach for 2-D problems; the specified wall flux and the symmetry/specular reflection boundary conditions are capable to handle specified q_w and suppressed dimensions; the boundary condition for mixed diffuse-specular surfaces is able to treat different surface properties. The 2-D Cartesian P_N and special boundary conditions are ready to be applied to more complicated applications such as simulations of real flames and reflections of real surfaces.

Acknowledgments

Support by National Science Foundation and the Department of Energy through Grant no. NSF-1258635 is gratefully acknowledged.

References

[1] J. Yang, M.F. Modest **High-order *P–N* approximation for radiative transfer in arbitrary geometries** *J Quant Spectrosc Radiat Transf*, 104 (2) (2007), pp. 217-227

[2] M.F. Modest, J. Yang **Elliptic PDE formulation and boundary conditions of the spherical harmonics method of arbitrary order for general three-dimensional geometries** *J Quant Spectrosc Radiat Transf*, 109 (2008), pp. 1641-1666

[3] M.F. Modest **Further developments of the elliptic** P_N-Approximation **formulation and its Marshak boundary conditions** *Numer Heat Transf B*, 62 (2–3) (2012), pp. 181-202

[4] W. Ge, R. Marquez, M.F. Modest, S.P. Roy **Implementation of high order spherical harmonics methods for radiative heat transfer on OpenFOAM** *ASME J Heat Transf*, 137 (5) (2015), p. 052701

[5] W. Ge, M.F. Modest, R. Marquez **Two-dimensional axisymmetric formulation of high order spherical harmonics methods for radiative heat transfer** *J Quant Spectrosc Radiat Transf*, 156 (2015), pp. 58-66

[6] Jasak H, Jemcov A, Tukovic Z. OpenFOAM: A C++ library for complex physics simulations. In: *International workshop on coupled methods in numerical dynamics*. Dubrovnik, Croatia IUC; 2007. p. 1–20.

[7] R.E. Marshak **Note on the spherical harmonics method as applied to the milne problem for a sphere** *Phys Rev*, 71 (1947), pp. 443-446

[8] M.F. Modest ***Radiative heat transfer*** (3rd edition), Academic Press, New York (2013)

[9] D.A. Varshalovich, A.N. Moskalev, V.K. Khersonskii ***Quantum theory of angular momentum*** World Scientific, Singapore (1981)

[10] J. Nocedal, S.J. Wright ***Numerical optimization*** (2nd edition), Springer-Verlag, Berlin (2006)

[11] W.H. Press, S.A. Teukolsky, W.T. Vetterling, B.P. Flannery ***Numerical recipes—the art of scientific computing*** (3rd edition), Cambridge University Press, Cambridge (2007)

[12] M.F. Modest **Photon-gas formulation of the differential approximation in radiative transfer** *Lett Heat Mass Transf*, 3 (1976), pp. 111-116